Lost Muons Analysis

FRANCESCO CONFORTINI
Supervisors: Anna Driutti, Brendan Casey

Abstract

The Muon g-2 experiment at FermiLab represents a significant scientific endeavor aimed at measuring the anomalous magnetic moment of the muon, a_μ, with a precision of 140 parts per billion (ppb). During my internship at FermiLab, I focused on the simulation and analysis of Lost Muons, a critical aspect to ensure the accuracy of the experimental results. I conducted a detailed study of the beam dynamics using the existing simulation, I generated a new simulation sample enrich of events with lost muons, I analyzed it and compared the results I obtained with those from the Run-2 dataset acquired by the experiment. In this report I will briefly describe my work, discuss the results and suggest future improvements.

1 Introduction: The Muon Anomalous Magnetic Moment

The magnetic moment of an elementary particle is equal to

$$\vec{\mu} = g\frac{q}{2m}\vec{S} \tag{1}$$

where q is the particle charge, m is its mass, and g is the so-called giromagnetic factor. The Dirac theory, the basis of the Standard Model (SM), predicts a value of $g = 2$ for any elementary particle of spin $\frac{1}{2}$, like the muon. Deviations from this value arise from radiative corrections (*i.e*, contributions from Quantum ElectroDynamics, ElectroWeak and QuantumChromoDynamics theory). This additional part, called the anomalous magnetic moment, is defined as:

$$a_\mu = \frac{g-2}{2} \tag{2}$$

Since the radiative corrections to a_μ are contributions from all possible particles, even hypothetical undiscovered particles, coupling to the muon via virtual loops, this makes every discrepancy between the theoretical value and the experimental measurement a good test for the SM [1]. A method to measure a_μ very precisely is based on the measurement of anomalous precession frequency (ω_a) of the muons in a constant magnetic field which, if there are no other electromagnetic fields, is defined as:

$$\vec{\omega}_a = \vec{\omega}_s - \vec{\omega}_c = a_\mu\frac{e\vec{B}}{m} \tag{3}$$

In details, for a relativistic particle the frequency at which the particle's momentum changes direction is called cyclotron frequency:

$$\vec{\omega}_c = \frac{q\vec{B}}{m\gamma} \tag{4}$$

where γ is the Lorentz factor. In addition, a particle with spin in the magnetic field $\vec{B}$ expe-

riences a torque which causes a precession motion of its spin around the direction of $\vec{B}$. The frequency of this precession is called Larmor frequency and can be expressed as:

$$\vec{\omega}_s = \frac{q\vec{B}}{m\gamma}(1 + \gamma a_\mu) \tag{5}$$

Hence, ω_a represents the frequency of the particle's spin precession relative to its momentum direction, as depicted in the Fig. 1. If g were equal to 2 the spin would always be parallel to the momentum direction and $\vec{\omega}_a = 0$, but since $g > 0$ by measuring ω_a and $\vec{B}$ we can measure a_μ [2].

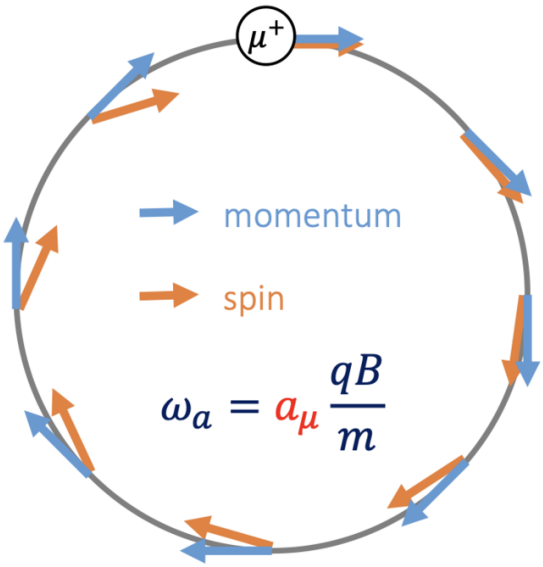

Figure 1: Schematic of the experimental technique used to precisely measure ω_a. [Picture taken from a colleague's talk].

This experimental technique is used by the Muon g-2 FNAL experiment which on August 10th, 2023 presented a new experimental measurement of ω_a from the analysis of the Run-2/3 datasets:

$$a_\mu^{FNAL} = 0.00116592057(24) \times 10^{-11}(210 \text{ ppb}) \tag{6}$$

With this new measurement, the world experimental average (*i.e*, the combination with the previous experimental measurements from BNL collaboration and FNAL Run-1) is:

$$a_\mu^{Exp} = 0.00116592059(22) \times 10^{-11}(190 \text{ ppb}) \tag{7}$$

All the experimental results are displayed in Fig. 2 [3].

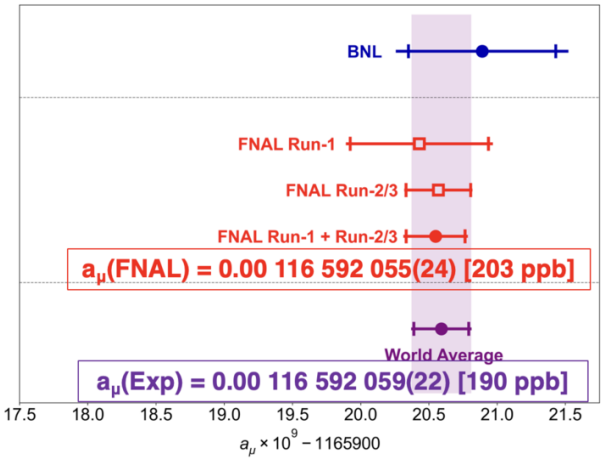

Figure 2: Experimental measurements of the muon anomaly from BNL and FNAL experiments, taken from [3].

2 Experimental Details

In the FNAL Muon $g-2$ experiment (E989) a polarized muon beam is produced from pion decay. In particular, the pions are produced

striking bunches of 8-GeV protons into a target. The positive 3.1-GeV/c pions are then extracted and transported trough the 279-m-long M2/M3 FODO beam line where about 80% of the pions decay into muons with an average longitudinal polarization of approximately 95%. The beam is then injected into a 505-m circumference Delivery Ring, where it circulates for four turns and the remaining protons and pions are swept out by an in-ring fast-kicker magnet. The purified and polarized muon beam is then injected into a 14.2 m-diameter superconductive storage ring characterized by a highly uniform 1.45 T magnetic field. The muons are left inside it to circulate for 700 μs and each individual injection sequence is called a "fill". Fig. 3 shows a schematic of the storage ring with all instrumentation.[4]

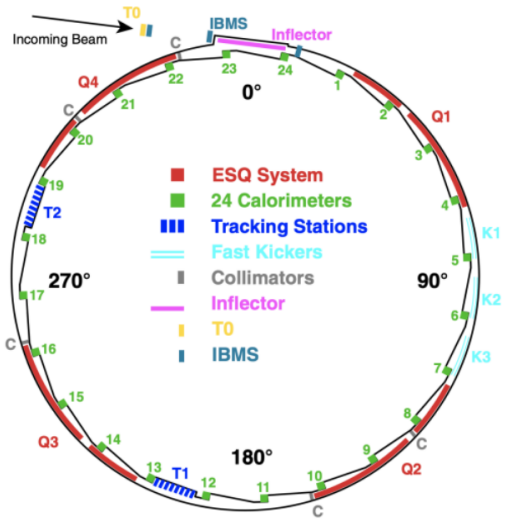

Figure 3: The storage ring of g-2, taken from [12].

The muons from the delivery ring enter the storage ring trough a nearly free field corridor provided by a superconductive magnet called inflector. Thanks to the inflector the particles avoid the deflections before entering the storage region but this step causes a large particle loss. At this point the injected beam is 77 mm off center but three kicker magnets (namely, K1,K2 and K3 in 3) provide a short, ideally less than 150 ns, but strong magnetic pulse that defect the muons passing trough them by $\approx$ 10 mrad.

While the muons circulate inside the ring, they decay. Positrons from muon decay are detected with a calorimeter system, consisting of 24 electromagnetic calorimeters positioned symmetrically around the inside radius of the storage ring, adjacent to the storage volume but outside of the vacuum chambers; see Fig. 4.

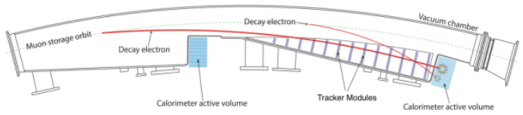

Figure 4: Schematics of the storage ring with two calorimeters and a tracker station, taken from [12].

Each calorimeter station consists of 54 crystals and silicon photomultiplier (SiPM) for the Cherenkov light read out. Positron showers are reconstructed offline and provide energy, time and impact position [5].

Two tracker stations, based on gas filled straw tubes are located inside the vacuum chamber at approximately 180° and 270° with respect to the inflector (as show in Fig. 4). They are used to trace back the positrons decay vertex and then reconstruct the positions of the muons inside the storage ring [6].

2.1 Master Formula

To precisely measure the muon anomaly a_μ the following expression is used [7]:

$$a_\mu = \frac{\omega_a}{\omega_p^{'}(T)} \frac{\mu_p^{'}(T_r)}{\mu_e(H)} \frac{\mu_e(H)}{\mu_e} \frac{m_\mu}{m_e} \frac{g_e}{2} \tag{8}$$

where the FNAL $g-2$ collaboration measures the ratio:

$$R_\mu \equiv \frac{\omega_a}{\omega_p^{'}(T_r)} \tag{9}$$

while the other constants, *i.e.*, the proton to electron magnetic moment ratio, the QED factor $\frac{\mu_e(H)}{\mu_e}$, the muon to electron mass ratio and the electron g-factor g_e, are obtained from calculation and external measurement [8].

The quantity R_μ in Eq. 9 can be written in terms of the measured quantity with the following expression:

$$R_\mu = \frac{f_{clock}\omega_a^m(1 + C_e + C_p + C_{ml} + C_{pa} + C_{dd})}{f_{calib}\omega_p^{'}(x,y,\phi) \otimes M(x,y,\phi)(1 + B_k + B_q)} \tag{10}$$

The denominator includes $\omega_p^{'}$ the magnetic field $\vec{B}$ seen by the muons expressed in terms of the field frequency maps calibrated using the f_{calib} factor and weighted by the muon distribution M [9].
The numerator includes the master clock blinding factor f_{clock}, the measured precession frequency ω_a^m and four beam-corrections C_i.
The measured anomalous precession frequency is extracting from the positive muons in the storage ring that decay following the reaction:

$$\mu^+ \rightarrow e^+ \nu_e \vec{\nu}_\mu \tag{11}$$

which is a weak decay that violates parity. Hence, positrons are emitted with an energy and an angular distributions strongly correlated to the muon spin direction in its rest frame. When boosted to the lab frame this correlation modulates the positrons energy spectrum at the ω_a rate and the total number of detected positrons seen by the calorimeter system (wiggle plot) can be described by the following 5 parameters function:

$$N(t) = N_0 e^{-\frac{t}{\gamma\tau_\mu}} \{1 + A(E)\cos[\omega_a t + \phi_0(E)]\} \tag{12}$$

where $\gamma\tau_\mu$ is the muons lifetime in the laboratory frame reference, $A(E)$ is the asymmetry, N_0 is the normalization, ϕ_0 is the phase and ω_a is the anomalous precession frequency. Therefore, in principle the value of ω_a can be measured by fitting with equation 12 the wiggle plot, *i.e.*, the number of positrons detected while the muons circulate in the ring [10].

2.2 Beam dynamics Corrections

In the ideal case the beam is in a perfect circular orbit, but in the real experiment the muons do not orbit in a perfectly horizontal plane in a homogeneous vertically magnetic field since they are vertically focused by a system of 4 electrostatic quadruples (ESQs) [11]. Moreover, during the measurement some muons leave the storage ring before decaying. To account for this effects, the following beam dynamics corrections are applied to ω_a^m in order to obtain ω_a [12]:

- C_e: to account for the muons that have momentum p different from $p_0 = 3.1\,\mathrm{GeV}/c$. It is extracted using the distribution of the equilibrium radii $x_e = x - R_0$, which is related to the momentum spread, $\Delta p = p - p_0$, since $\frac{\Delta p}{p_0} \approx x_e(1-n)/R_0$, where n is the field index determined by the ESQs operational voltage.

- C_p: the pitch correction is required to account for the vertical betatron oscillation that lead a non zero average value of $\vec{\beta} \cdot \vec{B}$. The correction formula is $C_p = n\langle A_y^2 \rangle / 4R_0^2$ where the acceptance-corrected vertical amplitude A_y is measured by the trackers.

- C_{pa}: the phase correction is required to account for the change in time of the phase term ϕ_0 in Eq. 12. It is evaluated by measuring the beam distribution with the trackers throughout the storage period and adding information from calorimeters' data and simulations.

- C_{dd}: the differential decay correction is required to account for the boosted lifetime of the high momentum muons with respect to the lower momentum muons.

- C_{ml}: the muon loss correction to account for the change during the fill of the phase ϕ_0 in Eq. 12 associated with muons lost since they have a slightly different spin phase compared to those that are stored.

3 Lost Muons and Simulation

In the experiment Lost Muons (LM) are those muons that while circulating into the $g-2$ ring are lost before decaying. In general, most of them are lost when they strike one of the circular collimator apertures that limit the transverse phase space admittance and its momentum dependence. Collimators (see figure 3 for their position around the ring) have an aperture of 45 mm radius and are centered in the middle of the vacuum chamber, the ideal orbits of the muons. Most of the muons are lost at early times after the injection, distorting the standard exponential decay. This effect is taken in account into the final ω_a fit including an additional factor $\Lambda(t)$ in Eq. 12:

$$N(t) = N_0 \Lambda(t) e^{-\frac{t}{\gamma\tau_\mu}} \{1 + A(E)\cos[\omega_a t + \phi_0(E)]\} \tag{13}$$

The additional factors is extracted from the loss function $L(t)$ which is the rate at which the muon are lost from the ring. The functional form of $\Lambda(t)$ can be expressed in term of $L(t)$ as:

$$\Lambda(t) = 1 - K_{ml} \int_0^t L(t') e^{t'/\gamma\tau_\mu} dt' \tag{14}$$

where K_{ml} is a scale parameter that is extracted from the fit analysis of the wiggle plot. The shape $L(t)$ is data-driven extracted using coincident signals in three consecutive calorimeter stations [10]. Coincidences are used since the lost muons signature is given by:

- Timing: muons travelling at speed of light cover the ≈ 1.8 m distance between two consecutive calorimeters in ≈ 6.5 ns.

- Energy: lost muons act like MIP particles, hence according to the Bethe-Bloch equation we expected that they a deposit they ≈ 170 MeV in the energy in each calorimeter that they crossed.

- Cluster hit multiplicity: differently from the positron showers, muons showers have a very localized energy just in 1 or 2 crystals in a calorimeter.

During my internship I studied the lost muons using simulation and compared my results with the lost muons spectra obtain with the data driven technique just described.

3.1 GM2RingSIM

In the experiment some of the corrections rely on simulations that describe the beam dynamics

and are cross-checked by performing comparison with the data. These data-simulation comparisons, first, they help to evaluate the robustness of the simulation software itself. Second, they allow to assess the realism and accuracy of the experimental technique employed.

The collaboration uses several compact simulation packages, in my internship I mainly used the GM2RingSim simulation which is a program based GEANT4 implemented within the ART framework [12, 13]. It includes the model of the storage ring (as show in Fig. 3) and uses as input a simulation of the beamline that steers the beam into the ring [14] to simulate the beam from injection into the storage ring trough storage and the interactions of the muons with materials and field. All the detectors, i.e., calorimeter and tracker systems are fully described, as well as the passive elements of the ring, such as the vacuum chambers with their inner structures, the ESQs, the kicker plates and the collimators.

The GM2RingSim simulation includes also some simulated detectors without material (called "ghost detectors") to track the particle journey in the ring without influencing it. In particular, the ghost detectors are the Lost Muon Ghost Detector (LMGD), a tube around the vacuum chamber used to detect the particles that leave the storage region, and the Ghost Tracking Planes (GTPs), which are 48 planes equispaced around the ring positioned orthogonal to the beam direction.

For the generation of the datasets the program includes several particle guns, each of which can generate datasets with different characteristics. In particular, during my internship, I used the Lost Muon Gun (LGM), which is set for the generation of high statistic simulation samples of lost muons.

4 The Lost Muon Gun Settings

The first part of my work involved understanding how the Lost Muon Gun works. This gun selects the muons that have more probability to be lost by calculating the maximum radius (r_{max}) that each muon could reach inside the ring. Only the muons with r_{max} above a chosen radius are not suppressed. The maximum radius is computed using the Twiss parameters as input.

The Twiss parameters are a set of fundamental parameters that characterize the shape and dynamics of a particle beam. These parameters provide crucial information about the beam's ellipse and emittance in the position-momentum phase space, both of which are important for understanding the beam behavior and its evolution [14].
For this reason as a first step I studied the ellipse that graphically represents the transverse cross-section of the particle beam in a specific time instant and is defined by two main parameters: the major axis β and the minor axis α. The β parameter is related with the maximum extent of the beam position (x or y) , while the α parameter to the maximum beam momentum rate of change (x' or y' defined in Eq. 19) [15]. Using β_x and α_x the equation of ellipse in $x - x^{'}$ phase space becomes:

$$\gamma_x x^2 + 2\alpha_x x x' + \beta_x x'^2 = \varepsilon_x \tag{15}$$

where γ_x is defined as:

$$\gamma_x = \frac{1 + \alpha_x^2}{\beta_x} \tag{16}$$

and the emittance ε_x represent the area of the ellipse in the $x - x'$. Similar definitions are used for the $y - y'$ phase space:

$$\gamma_y y^2 + 2\alpha_y y y' + \beta_y y'^2 = \varepsilon_y. \tag{17}$$

with:

$$\gamma_y = \frac{1+\alpha_y^2}{\beta_y} \tag{18}$$

and ε_y the area of the ellipse in the $y - y'$ phase space.

To better understand the beam dynamics and the Twiss parameter I analyzed a simulated test sample based on Run-2 settings. Fig. 5 and Fig. 6 show the distributions of the particle beam in the phase space for the radial $(x - x')$ and the vertical $(y - y')$ directions.

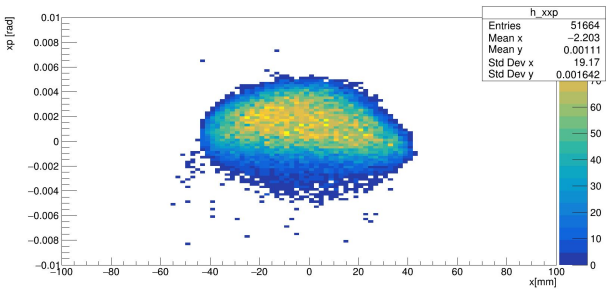

Figure 5: Beam distribution in the radial phase space $(x - x')$ when the muons are starting the 10^{th} turn in the ring.

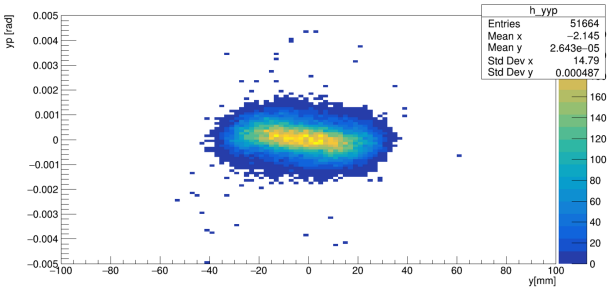

Figure 6: Distributions in the vertical phase space $(y - y')$ when the muons are starting the 10^{th} turn in the ring.

These distributions are taken analyzing the simulated positions of the muons in the GTP0 (placed just right after the injection at 0° in Fig. 3). In the x-axis is reported the radial or vertical position of the muons while in the y-axis is reported x' and y', which are defined as:

$$x' = \frac{p_{radial}}{p_{logitudinal}} \qquad y' = \frac{p_y}{p_{logitudinal}} \tag{19}$$

The 1-Dimension distributions of each of these observables, *i.e.*, x, x', y, y' for the 10^{th} turn as recorded on the GTP0 are show in Fig. 7 and Fig. 8.

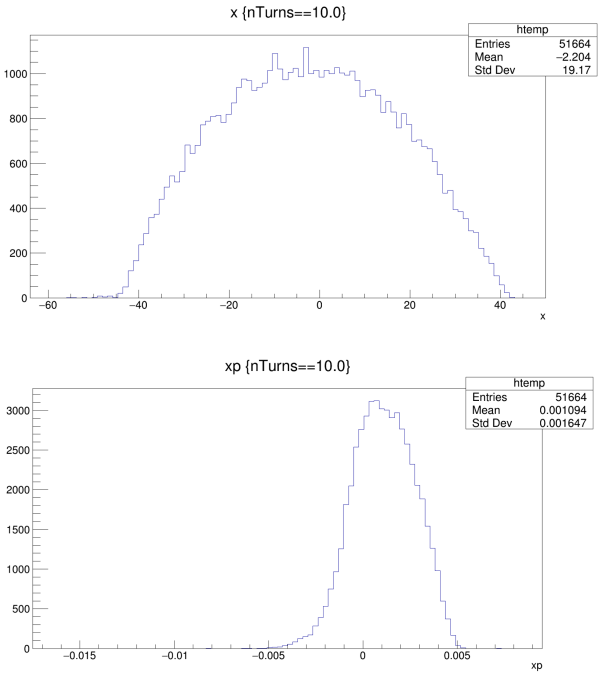

Figure 7: Distribution for (top) x (express in millimeters) and (bottom) for x' (expressed in radians).

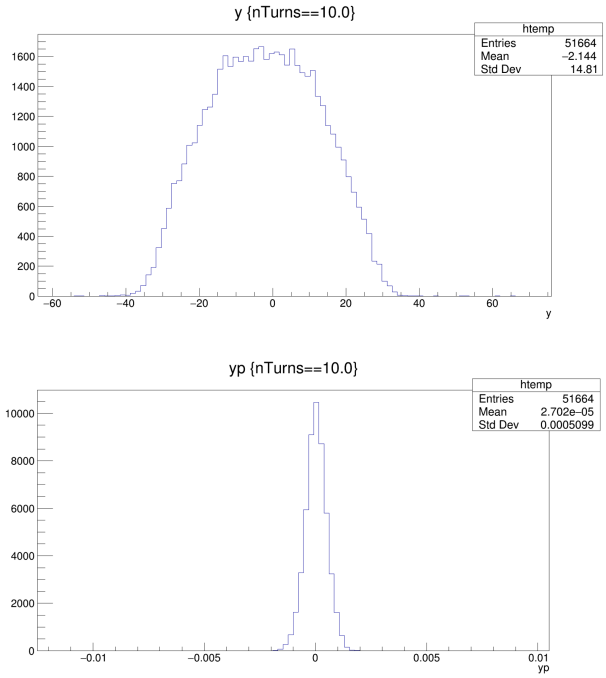

Figure 8: Distribution for (top) y (express in millimeters) and (bottom) for y' (expressed in radians).

The distributions observed don't have a Gaussian shape. Therefore, for the calculation of the emittance, I employed the definition of the root mean square emittance defined as:

$$\varepsilon_{xrms} = \sqrt{\langle x^2 \rangle \langle x'^2 \rangle - \langle x \cdot x' \rangle} \qquad (20)$$

where $\langle x^2 \rangle$ is the variance of the particle's position shown on top of Fig. 7, $\langle x'^2 \rangle$ is the variance of the angle that the particle makes with the direction of travel shown on bottom of Fig. 7, while $\langle x \cdot x' \rangle$ represents an angle-position correlation of particles in the beam. Same definition was used for y-space by using the variance of the distributions in top and bottom of Fig. 8. The results obtained are showing in table 1:

ε_x [mrad]	β_x [m]	γ_x[m^{-1}]	α_x
$31.14 \cdot 10^{-6}$	11.79	0.86	0.14
ε_y [mrad]	β_y [m]	γ_y [m^{-1}]	α_y
$7.04 \cdot 10^{-6}$	31.16	0.036	0.22

Table 1: Summary of the ellipse parameters in $x - x'$ and $y - y'$ phase-space.

Fig. 9 and Fig. 10 show the ellipses obtained with these parameters superimposed to the simulated beam distributions.

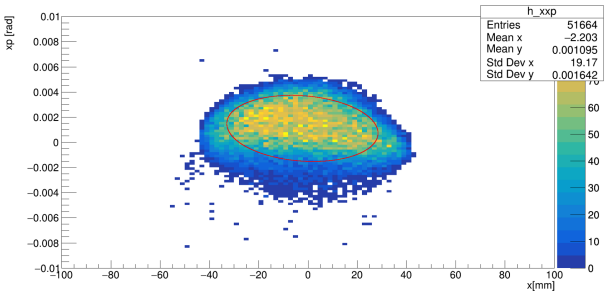

Figure 9: Distribution of Fig. 5 with superimposed the ellipse obtained with the parameters described in the top part of Table 1.

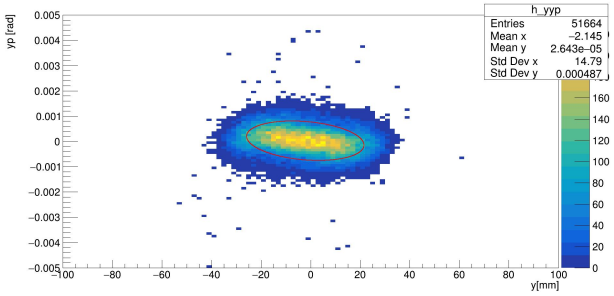

Figure 10: Distribution of Fig. 6 with superimposed the ellipse obtained with the parameters described in the top part of Table 1.

We can see that the ellipse from our analysis aligned well with the beam shape's and characteristics.

I crossed check the parameters of Table 1 with the parameters calculated from considering the beam as perfectly injected (provided by a colleague). Comparison is shown in tables 2 and 3.

β_x [m]	α_x	γ_x [m^{-1}]
11.79	0.14	0.86
β_{xC} [m]	α_{xC}	γ_{xC} [m^{-1}]
7.67	0.017	0.13

Table 2: Comparison of $x - x'$ parameters extracted by the full simulation with ideal injection calculations.

β_y [m]	α_y	γ_y [m^{-1}]
31.16	0.22	0.036
β_{yC} [m]	α_{yC}	γ_{yC} [m^{-1}]
21.22	-0.038	0.047

Table 3: Comparison of $y - y'$ parameters extracted by the full simulation with ideal injection calculations.

The difference is due to the fact that the parameters from the full distribution contain the momentum dispersion of the beam [15], *i.e.*, the simulation accounts for the spread in momentum at injection. In the Lost Muon Gun we used the parameters from the calculations (β_C, α_C, γ_C from tables 2 and 3) as input to evaluate r_{max} since the code already accounts for the effects of the realistic injection. Beside the Twiss and dispersion parameters I also set the rejection radius to 38 mm so that all the particles which are expected to be stored *i.e.*, to have $r_{max} < 38$ mm are suppressed. With these parameters and the Run-2 configuration I simulated a sample of $8.98 \cdot 10^8$ muons. Details are given in section 5.

5 Dataset Generation with the Lost Muon Gun

To begin with, the first step involved the generation of a simulated dataset using the Lost Muon Gun, which is designed to create datasets with a high number of lost muons. Notably, for its operation, it requires the Twiss parameters specific to the beam as input. These parameters are crucial for simulating the motion of muons while are in the ring, ensuring that the simulation accurately reflects the desired characteristics and to select the muons with the highest probability to be lost. As previously explained although, the parameters we previously extracted matched the Run-2 simulated beam shape well, we use to select the high probable to be lost muons the parameters from calculations with perfect injected beam since the effect of the injection are accounted by the code in the simulation. Figure 11 shows the total number of events I produced using the FermiGrid [16] with the Lost Muon Gun set as described previously.

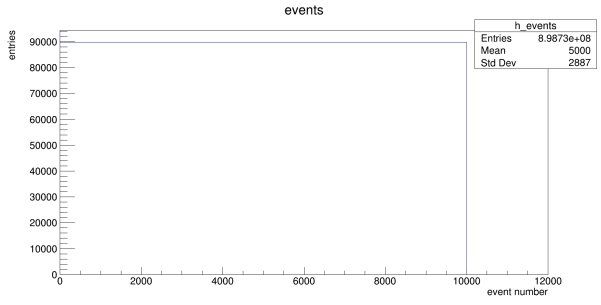

Figure 11: Total number of events I generated.

The final sample generated contained almost 10 billion events in which one muon is traced from injection up to 700 μs. In particular, we set the Lost Muon Gun with the Run-2 experimental settings *i.e.*, same time and spatial distributions of the beam before injection, same ESQs, kicker and magnetic fields as measured experimentally. To better monitor the behavior of lost muons within the ring, especially their interactions with collimators and coincidences with calorimeters, we adjusted the muon decay time inside the ring. This adjustment significantly extended the muon lifetime within the ring, enabling all muons to complete many more revolutions. This allowed for a more statistics and hence a more detailed observation of their interactions even if due to this change in the simulation muon lifetime parameter, we deliberately did not account for potential background signals stemming from triple coincidences of positrons resulting from muon decays in the calorimeters. Hence, the modification of the muon decay time aimed to isolate and concentrate on the specific behaviour of the lost muons, eliminating interference from such background signals.

6 Lost Muons Analysis

After producing a simulation sample I wrote a module to perform the lost muons analysis which has the objective to select and to gain insight into the behaviour of the muons that are lost.
First, I define the muons as lost using the distance from the center of the ring to the center of the storage region: $r_{Magic} = 7112\,\text{mm}$, and the radius of the storage region $r_{Storange} \approx 50\,\text{mm}$. Therefore defining:

$$r = \sqrt{x^2 + z^2} - r_{Magic} \tag{21}$$

we can say that a muon is lost if:

$$\sqrt{r^2 + y^2} > r_{Storage} \tag{22}$$

Then, I tagged assigning $CollimatorsHit = 1, 2, 3, ...$, the lost muons that hit 1,2,3,... times one (or more) of the 5 collimators in the ring. If a muon hits a collimator is highly probably that it will be lost.
Figures 12, 13, 14, 15 and 16 show the distributions of the position where the muons hit each collimator, namely collimators 2, 3, 6, 8 and 9. In these plots r coordinate is calculated as Eq. 21 *i.e.*, the radial distance from the center of the vacuum chamber, while the y is the vertical distance.

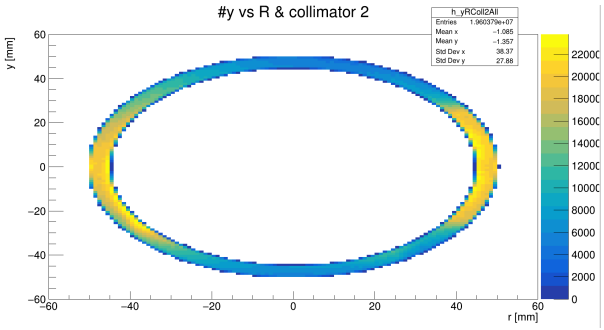

Figure 12: Muon hit positions in Collimator 2.

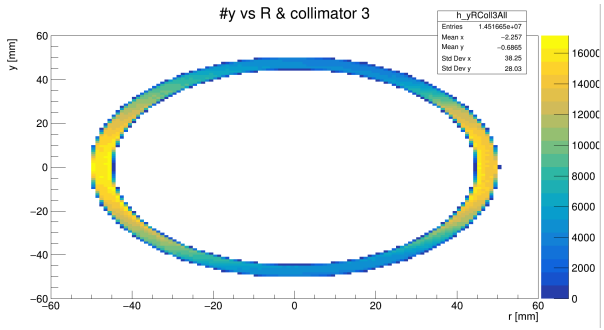

Figure 13: Muon hit positions in Collimator 3.

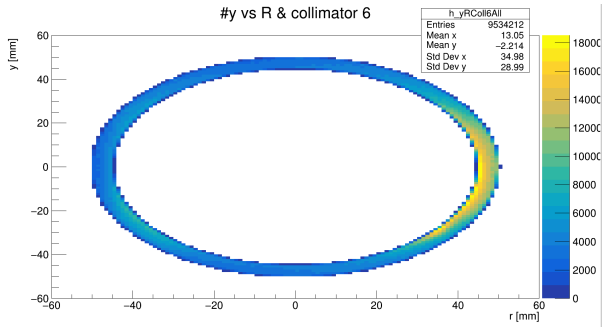

Figure 14: Muon hit positions in Collimator 6.

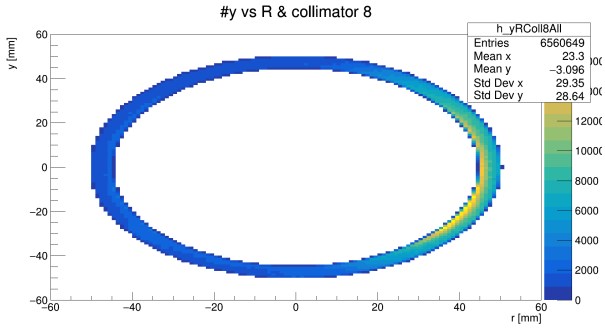

Figure 15: Muon hit positions in Collimator 8.

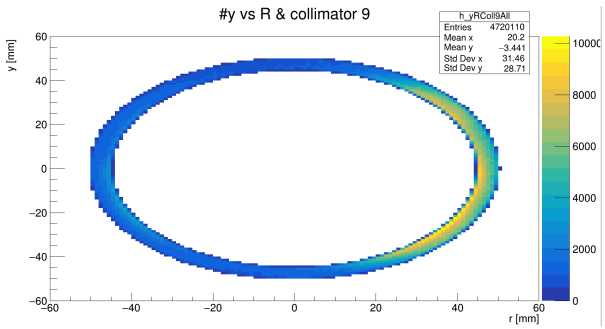

Figure 16: Muon hit positions in Collimator 9.

The distributions for collimators 2 and 3, which are located closer to the entrance of the ring, exhibit a right-left side symmetry. In contrast, the distributions of collimators 6, 8 and 9 which are positioned near the end of the ring, appear more concentrated on the right side. We are still investigate this effect.

Figures 17, 18, 19, 20 and 21 show the previous distributions but with muons that survive in the ring for $> 10\,\mu$s (top) and $> 30\,\mu$s (bottom). We see that the majority of the muons was lost in the early times right after the injection. The one the survive at least $10\,\mu$s hit mostly the right (towards the outer side ring) side of the collimator, while the survivors after $30\,\mu$s hit the collimators surface more homogeneously.

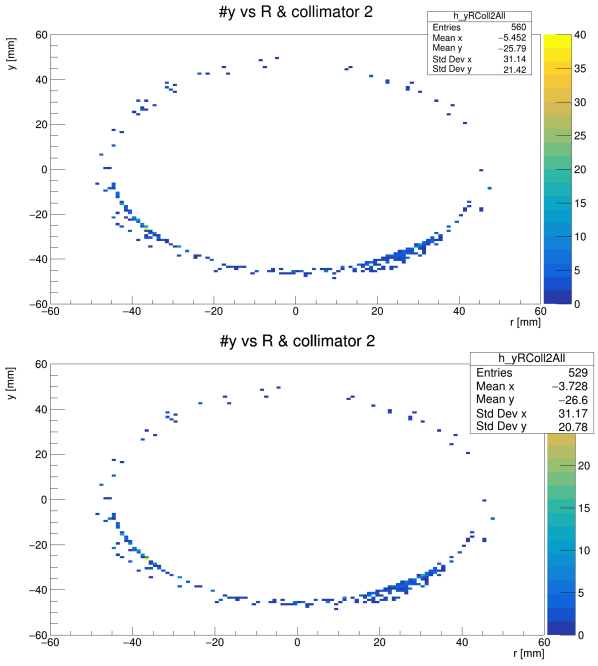

Figure 17: Muon hit positions in Collimator 2 for survivors (top) $> 10\,\mu$s and (bottom) $> 30\,\mu$s.

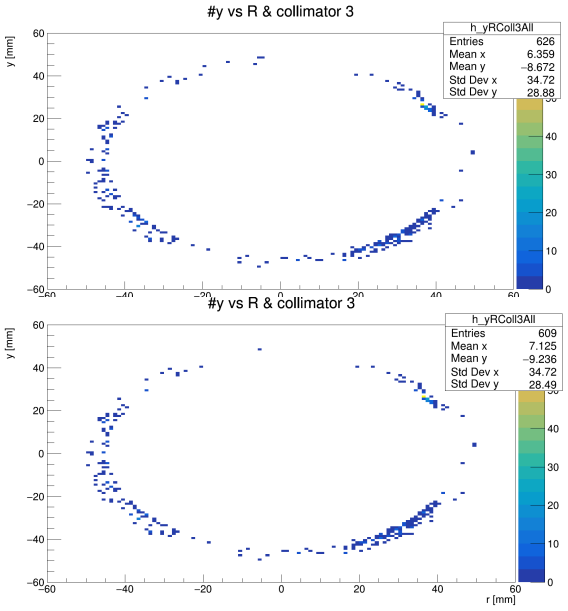

Figure 18: Muon hit positions in Collimator 3 for survivors (top) $> 10\,\mu$s and (bottom) $> 30\,\mu$s.

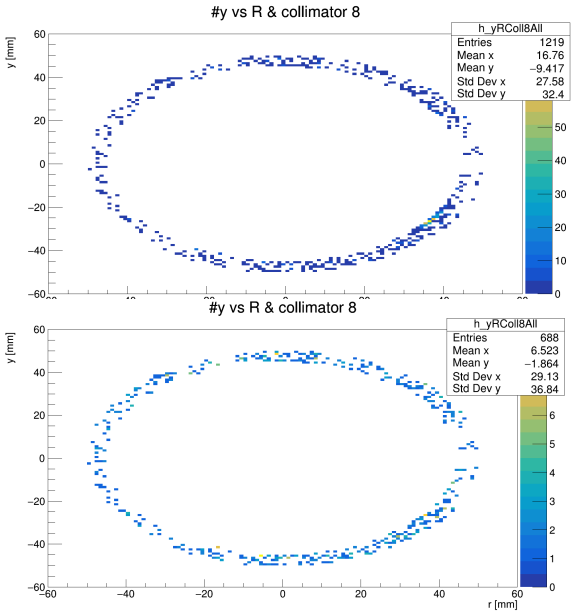

Figure 20: Muon hit positions in Collimator 8 for survivors (top) $> 10\,\mu$s and (bottom) $> 30\,\mu$s.

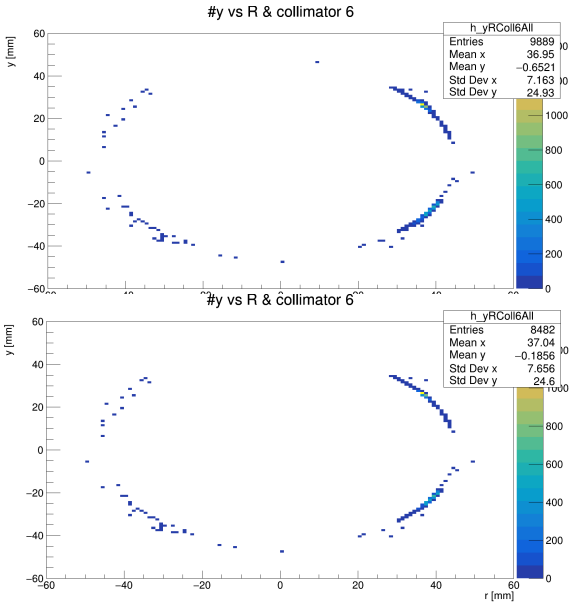

Figure 19: Muon hit positions in Collimator 6 for survivors (top) $> 10\,\mu$s and (bottom) $> 30\,\mu$s.

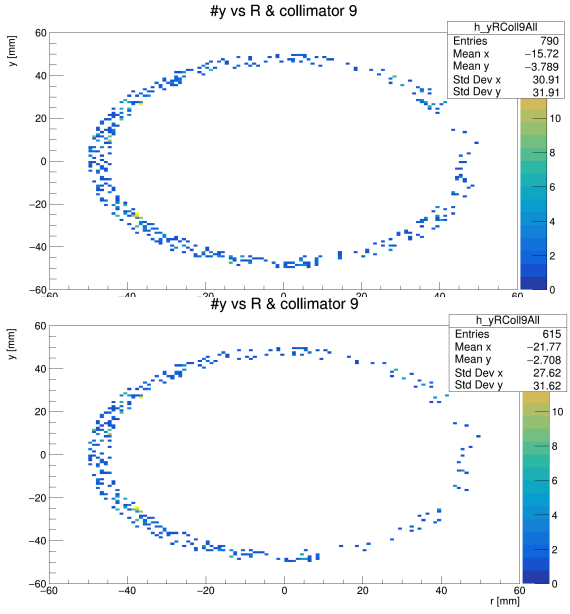

Figure 21: Muon hit positions in Collimator 9 for survivors (top) $> 10\,\mu$s and (bottom) $> 30\,\mu$s.

In contrast, when we analyzing real data, we employed a model based on triple coincidences with the calorimeters. We then tag with $CaloCoincidence = 2, 3, 4$ the muons that exit the storage region and make a double or triple or quadrupole coincidence in the calorimeter system. Figure 22 shows the muon tagging: on the y-axis the number of calorimeter coincidences, while in the x-axis the number of times the muon hit a collimator for all the muons (top), the muons that survive $> 10\,\mu$s (middle) or $> 30\,\mu$s (bottom)inside the ring.

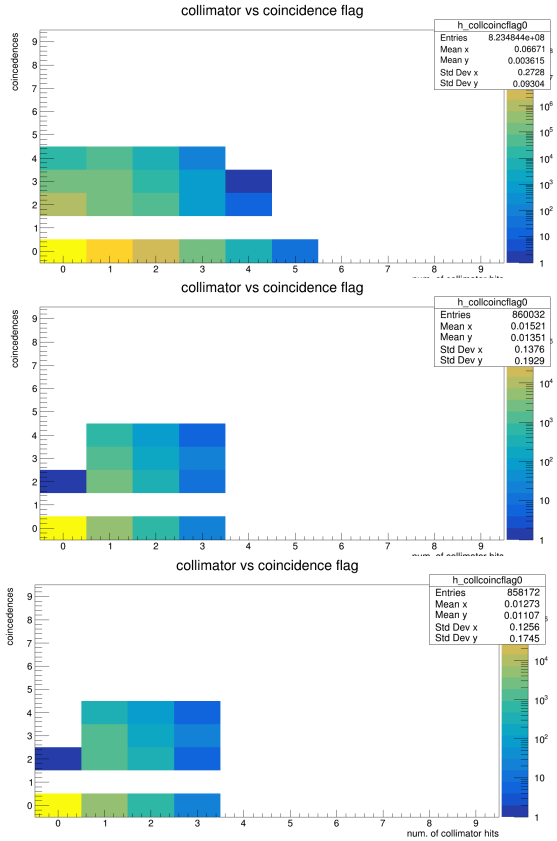

Figure 22: $CaloCoincidence$ vs $CollimatorHits$ for (top) all muons, (middle) survivors $> 10\,\mu$s and (bottom) survivors $> 30\,\mu$s.

We see that for the muons that survive at least 10μs (*i.e.*, Fig. 22 middle and bottom) only the muons that hit a collimator make a triple or more coincidence in the calorimeter system.

With these definitions we can study the lost muons using a different approach, which is tailored to the characteristics of the experimental setup and the data collected. This is because, in the analysis of real data, we are unable to tag muons that have interacted with a collimator. Therefore, our aim is to compare these two definitions of "lost muons" using the simulation as a bridge. By doing so, we asses how the simulation's definition of lost muons, which includes information of the interactions with collimators, aligns with the definition based on triple coincidences with calorimeters used in the analysis of real data, by studying the distribution of the muons when they interact with a collimator and compare it with those that make double or multiple coincidences in the calorimeters. Moreover, we analyzed and compared the temporal spectra of decaying muons, $L(t)$ (see Sec. 3), both for those that interact with a collimator and those that undergo triple coincidences in the calorimeters.

Furthermore, we analyzed the time intervals between double, triple, and quadruple coincidences, and the first and the last collimator hit. Finally, the same analysis has been perform selecting the muons that are in the ring in the time intervals 0-700 μs, 10-700 μs and 30-700 μs. The last time interval coincides with the one used to perform the fit to extract ω_a^m.

6.1 Lost Muon Position

Initially, I studied the position of the muons within the ring, as show in Figure 23 where the muon's position within the ring as a function of

the turn performed by the muon is illustrated. Of particular interest are the events involving muons that, during the simulation, exceed a displacement of 45 mm within the ring and circulate in the ring at least for 30 μs ($\sim$ 200 turns). These muons are called "Edge muons" since they have the possibility to interact with a collimator and subsequently exit the vacuum chamber.

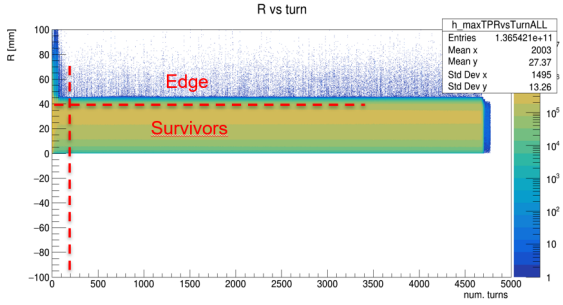

Figure 23: Radius of the muons during their path inside the ring with the definition of Edge and Survivors.

Figure 24 displays the positions at which muons leave the storage ring. This information is extracted using the LMGD described in Sec. 3.1.

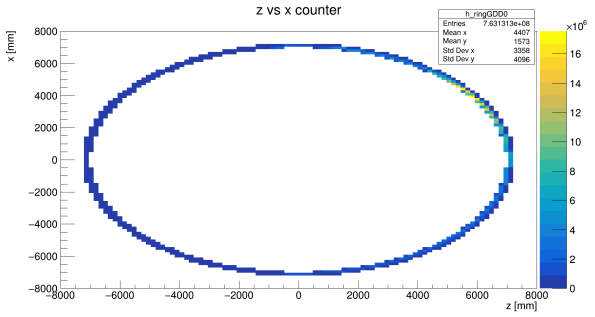

Figure 24: Positions where muons exit the storage ring.

It is evident that the majority of events are lost in the initial region of the ring, particularly in proximity of the kicker region.

Figures 25, 26 and 27 show the positions, detected with the LMGD, where muons that have hit a collimator exit the vacuum chambers.

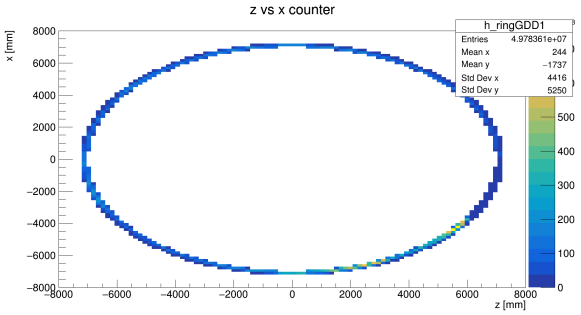

Figure 25: Positions at which muons that hit the collimators exit the storage ring.

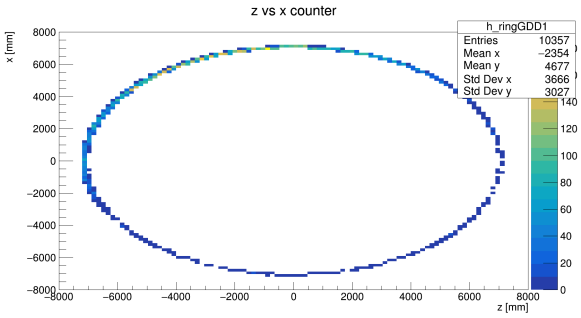

Figure 26: Positions at which muons that hit the collimators exit the storage ring after 10 μs.

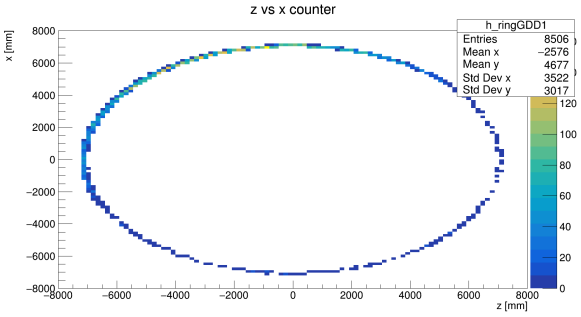

Figure 27: Positions at which muons that hit the collimators exit the storage ring after 30 μs.

We observe that for the muons that survive inside the ring for at least 10 and 30 μs, the majority of them are lost in the last quadrant of the ring (after all five collimators). While the majority of the muons that exit before 10 μs leave the ring in the second quadrant, after the first two collimators. For the position of the five collimators refer to Figure 3.

6.2 Coincidens and Collimators

In the Figures 28, 29 and 30 are shown the number of triple coincidences made versus the number of the first calorimeter hit in the triple. Each figure shows a distribution with a different time-interval: 0-700 μs, 10-700 μs and 30-700 μs.

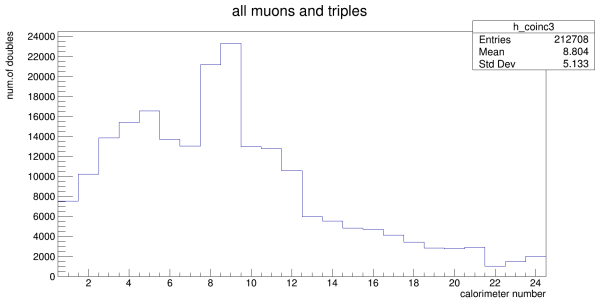

Figure 28: Triple coincidences vs number of first calorimeter hit during 0-700 μs.

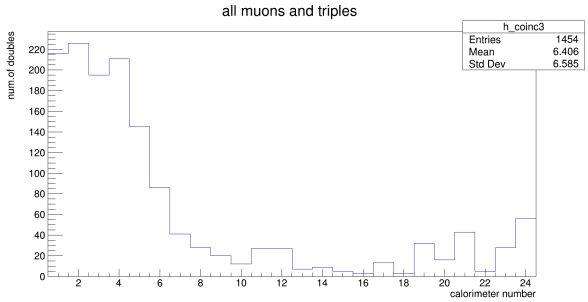

Figure 29: Triple coincidences vs number of first calorimeter hit during 10-700 μs.

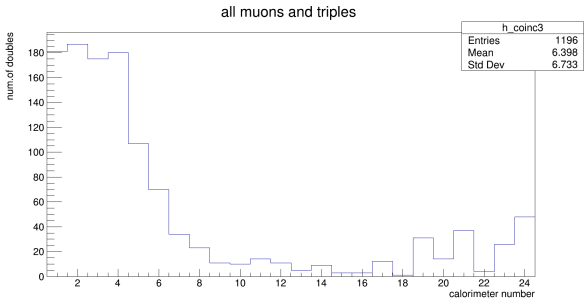

Figure 30: Triple coincidences vs number of first calorimeter hit during 30-700 μs.

It can be seen that of all muons that make a triple coincidence only the 0.68% makes a coincidence after 10 μs.

Figures 31, 32, 33, 34, 35, 36 show the distributions of the momentum respectively for the muons that hit a collimator and for the one that make at least a double coincidence. In these distributions the momentum is defined as the momentum of the muon when hits the last GTP before exiting the storage region substract and divided by the momentum which muons should have if they don't interact with the maerial in the ring:

$$\Delta p = \frac{(p_{lastGTP} - p_{magic})}{p_{magic}}. \qquad (23)$$

These distributions are compared with the one coming from the muons that neither make a coincidence nor hit a collimator; see Figures 37, 38 and 39. All of them are taken with the usual different time-intervals: 0-700 μs, 10-700 μs and 30-700 μs.

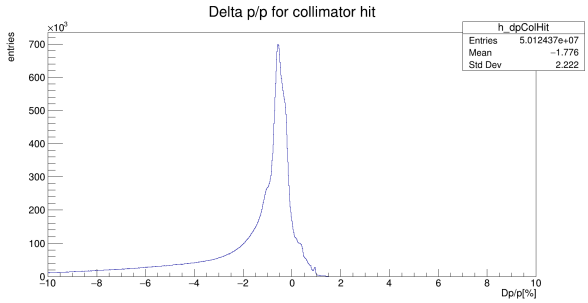

Figure 31: Δp distribution of muons that hit a collimator.

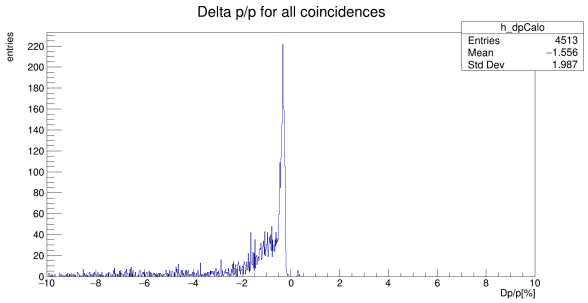

Figure 34: Δp distribution of muons that make a coincidences and survived $> 10\,\mu$s.

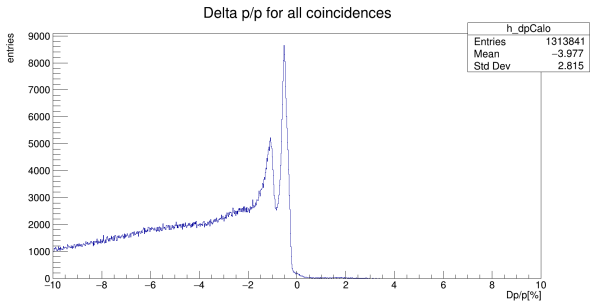

Figure 32: Δp distribution of muons that make at least a double coincidence.

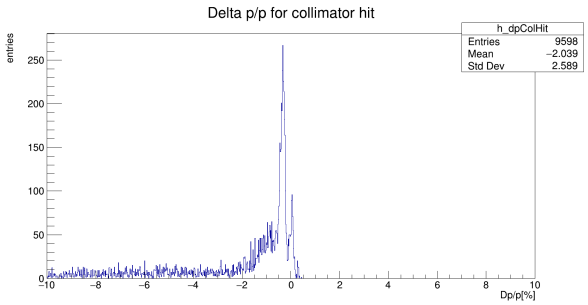

Figure 35: Δp distribution of muons that hit a collimator and survived $> 30\,\mu$s.

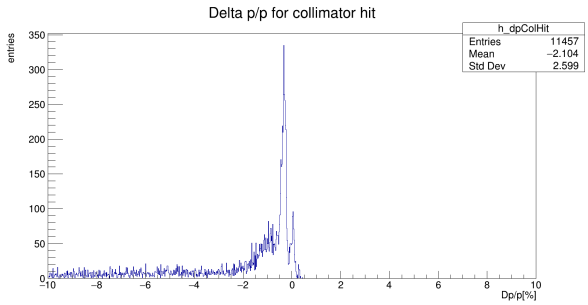

Figure 33: Δp distribution of muons that hit a collimator and survived $> 10\,\mu$s.

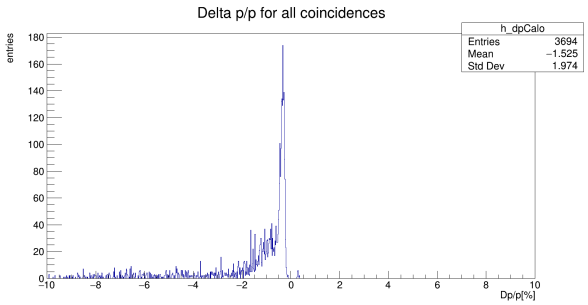

Figure 36: Δp distribution of muons that make a coincidences and survived $> 30\,\mu$s.

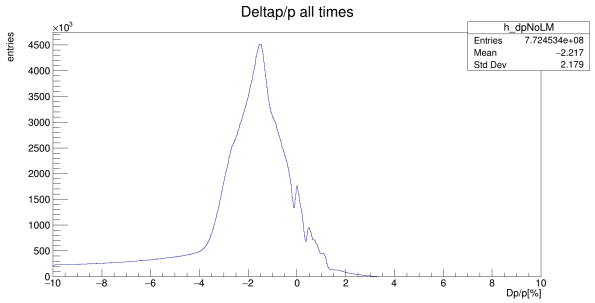

Figure 37: Δp distribution of muons that neither make a coincidence nor hit a collimator.

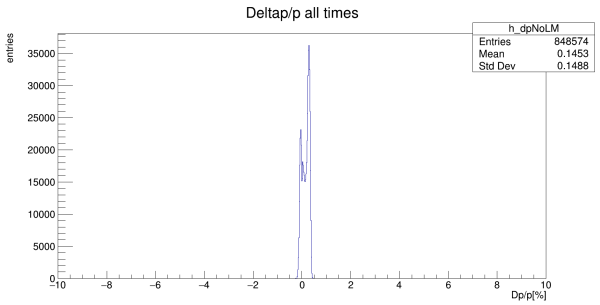

Figure 38: Δp distribution of muons that neither make a coincidence nor hit a collimator and survived $> 10\,\mu$s.

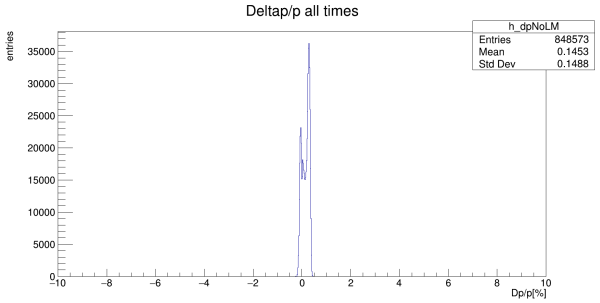

Figure 39: Δp distribution of muons that neither make a coincidence nor hit a collimator and survived $> 30\,\mu$s.

Finally, Figures 40, 41 and 42 show the distributions of the momentum defined as in Eq. 23 for muons with the different coincidence multiplicity, *i.e.*, doubles, triples, and quadruples. In each figure on the top, middle, bottom are shown the distributions for the time-intervals 0-700 μs, 10-700 μs and 30-700 μs, respectively.

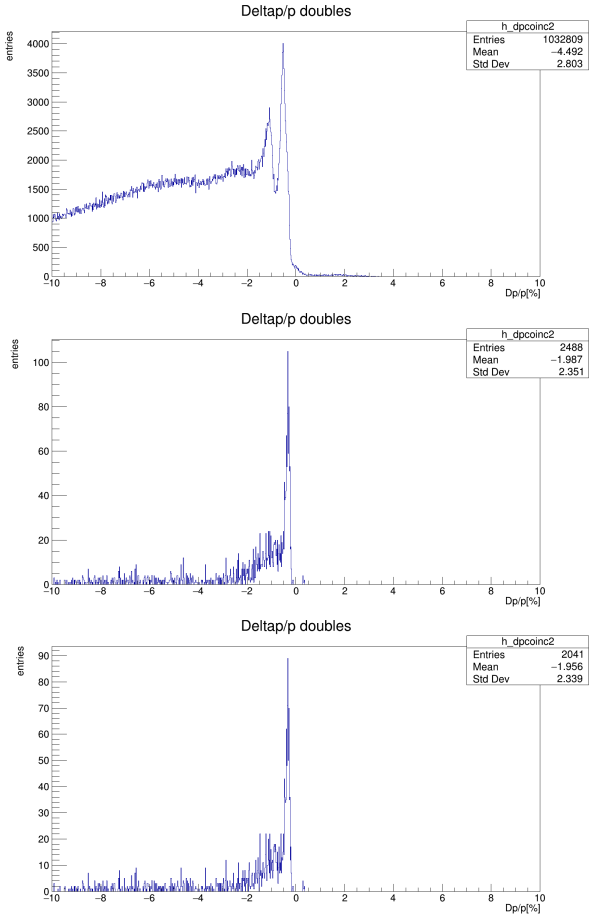

Figure 40: Δp distribution of muons that make a double coincidence after (top) 0 μs, (middle) 10 μs and (bottom) 30 μs.

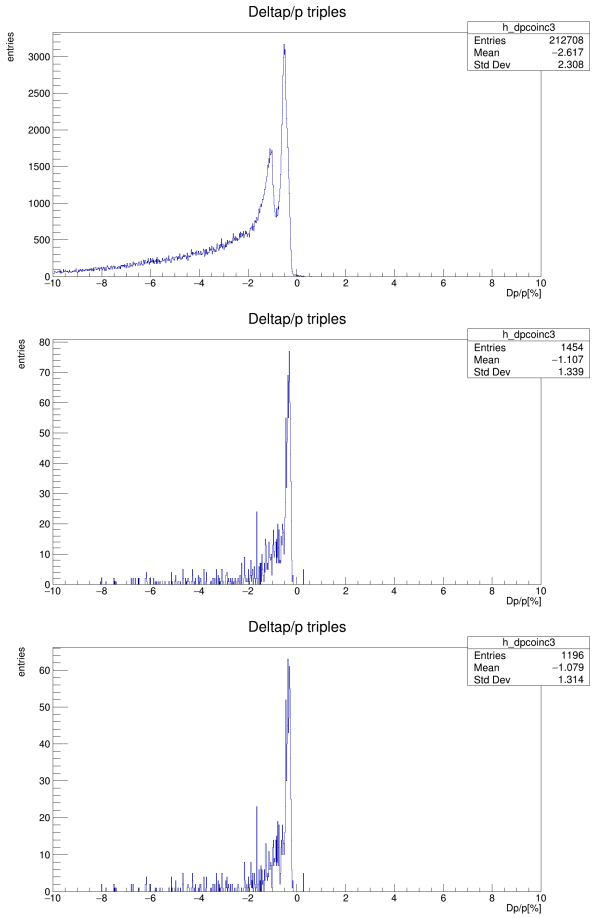

Figure 41: Δp distribution of muons that make a triple coincidence after (top) 0 μs, (middle) 10 μs and (bottom) 30 μs.

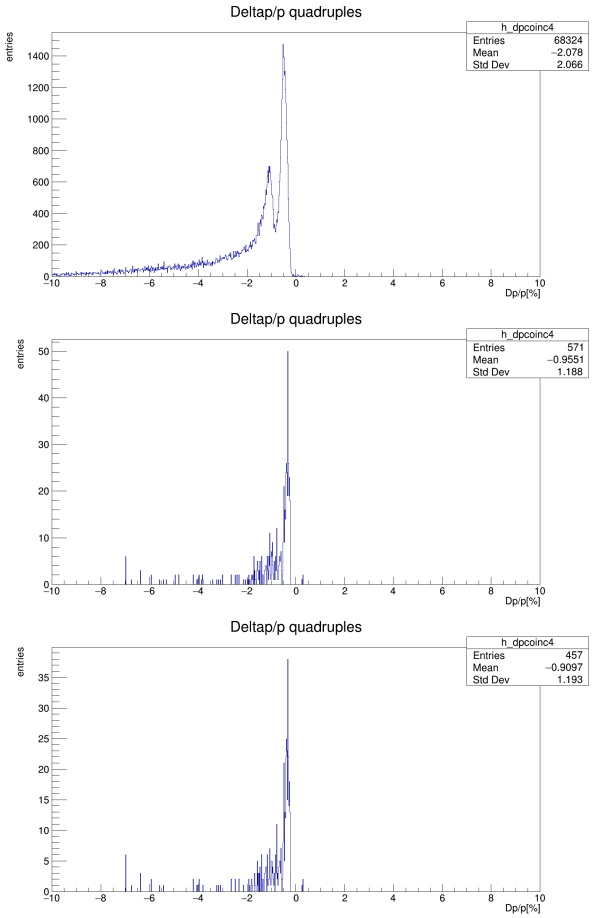

Figure 42: Δp distribution of muons that make a quadruple coincidence after (top) 0 μs, (middle) 10 μs and (bottom) 30 μs.

A low momentum tail is visible in all distributions. We think it is populated by the muons that interact with the material in the ring during the initial scraping in the inflector and/or by hitting collimators, kickers and quadrupoles plates. These possible causes of the momentum lost are under investigation.

Figures 43 and 44 show the the time distance between the first and last collimator hits as a function of the time and the turns that muons stays in the ring, respectively.

From this distribution we can see that muons can travel inside the ring for even for ≈ 4000 turns between the first and the last time they hit a collimator.

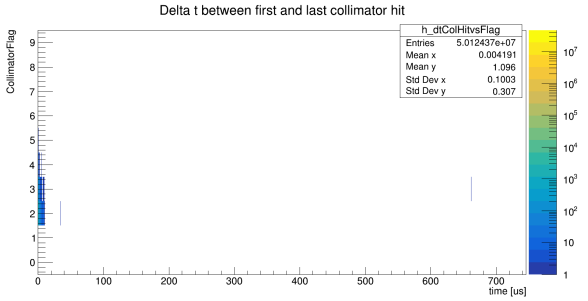

Figure 43: Time distance between the first and last collimator hits versus time the muon exits the storage ring.

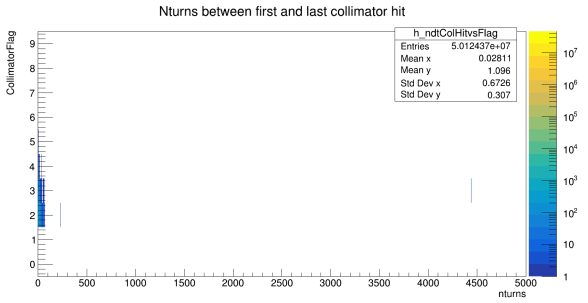

Figure 44: Time distance between the first and last collimator hits versus number of turn the muon does in the ring.

Figures 44 and 45 shows the difference time between the triple coincidence and both the first and last collimator.

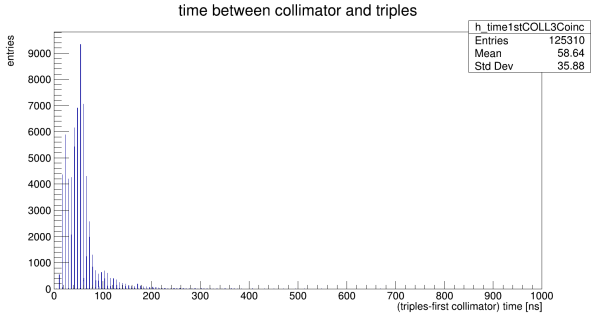

Figure 45: Time difference between the first collimator hit and the triple coincidence in the calorimeter system.

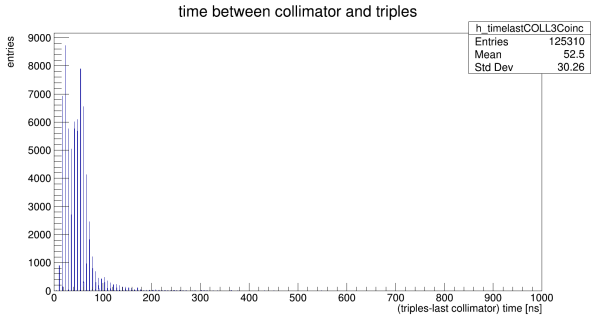

Figure 46: Time difference between the last collimator hit and the triple coincidence in the calorimeter system.

These distribution show that most of the muons travel for less than $\approx$ 100 ns from the collimator hit (both first and last) before be detected as a triple coincidence in the calorimeter system. Similar difference in time as been found considering the lost muons that are detected as a quadruple coincidences, but seams that the time interval between collimators first or last hit and double coincidence in the calorimeter is slighty shorter (see Figures 47 and 48).

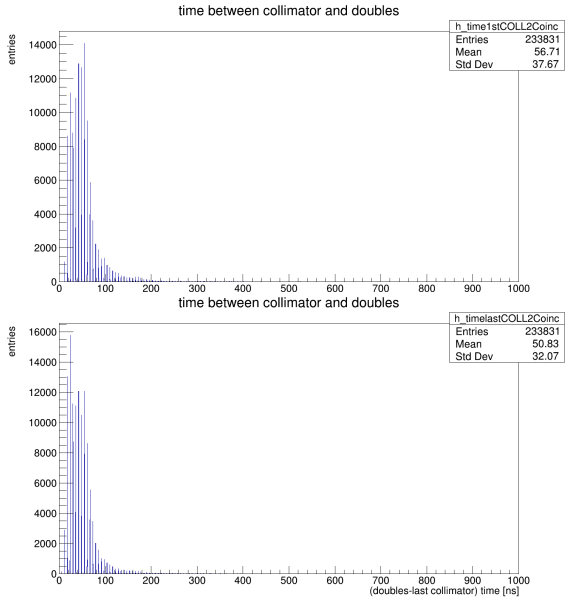

Figure 47: Δt between the (top) first and (bottom) last collimator hit and the doubles.

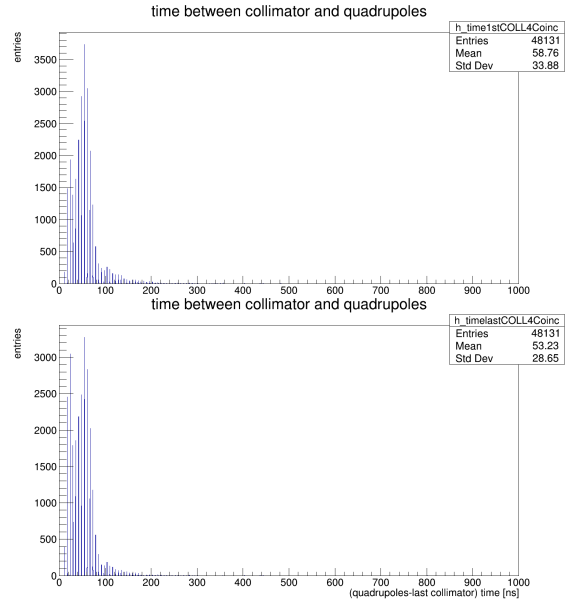

Figure 48: Δt between the (top) first and (bottom) last collimator hit and the quadruples.

6.3 Comparison with the real data

One of the goals of the lost muons analysis is to compare the simulated lost muons with the data-driven.

Figure 49 illustrates the temporal spectra $L(t)$ (see Sec. 3) of the muons simulated and defined using the triple coincidences in the calorimeter system. In comparison, figure 50 shows those muons defined as lost because they interact with the collimators.

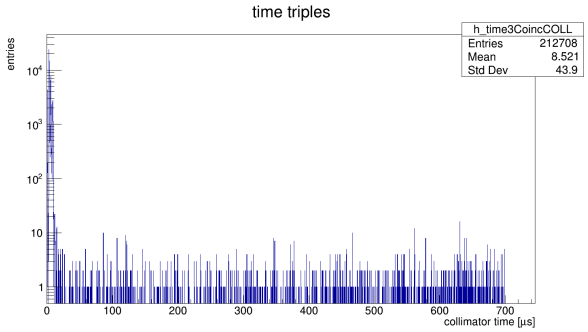

Figure 49: $L(t_{GTPs})$ of lost muons detected with the calorimeter triple coincidences in simulation.

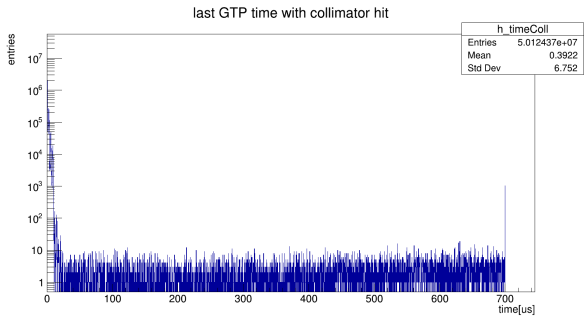

Figure 50: $L(t_{GTPs})$ for lost muons tagged with the collimator hits.

In these two plots the time is defined as the last time recorded by the GTPs in the simulation (t_{GTPs}). We can see that both spectrum have very similar behaviour except for the peak at 700 μs in Fig. 50 which represents the muons that hit a collimator but never leave the storage ring (within the simulation time-frame that is 700 μs, see Sec. 5 for details). As said, the final goal is to compare these two distributions with the time spectrum coming from the experimental data taken during Run-2 and shown in Figure 51.

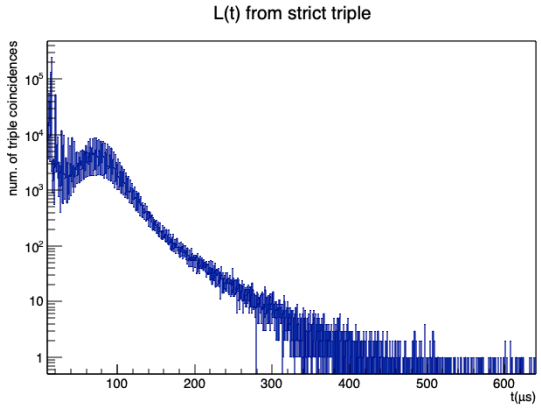

Figure 51: $L(t)$ from Run-2 lost muon experimental data [Courtesy of ω_aEuropa Group].

At the present statistic in simulation is still not enough for this comparison, Also, in simulation the exponential behaviour is missing since as previously explained the muon decay was suppressed when the dataset has been generated. The statistical limitation primarily arises from the fact that a significant portion of muons are lost, as expected, during the initial few microseconds of their journey in the ring. In fact only 1-2% of the muons stay inside the ring for more than 30 μs (this is similar to the experimental acceptance [12]).

Finally, Figure 52 shows the comparison between simulation and experimental data collected during Run-2 of the number of triple coincidences recorded for each calorimeter after 30 μs. The simulation seams to reproduce the peak of coincidences seen on the first 8 calorimeters but also this comparison is limited by the low statistics sample of the simulation.

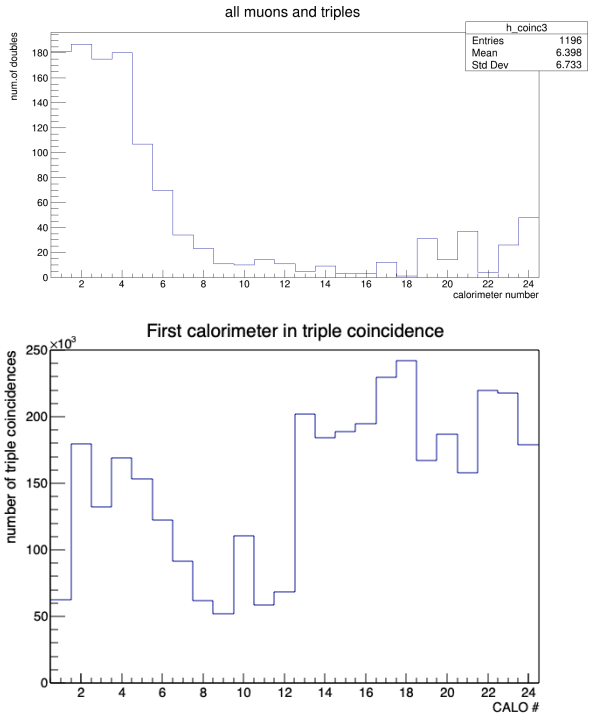

Figure 52: Comparison of the number of triple coincidences recorded for each calorimeter after 30 μs between (top) simulation and (bottom) experimental data taken during Run-2 [Experimental data courtesy of ω_aEuropa Group].

Therefore, our future plans include a continued effort to generate a more substantial dataset, with the aim of investigating and understanding the lost muons more comprehensively.

7 Conclusions

These two months at Fermilab have been an extraordinary learning experience, during which I delved into the intricacies of the $g-2$ experiment, particularly with respect to the beam dynamics corrections. I gained valuable insights into utilizing simulations for generating datasets with a high number of Lost Muons and leveraging simulation tools for the subsequent data analysis. Furthermore, I acquired the knowledge to compare simulation results with those obtained from real data, allowing for an assessment of the model's consistency and the adequacy of the simulation. This opportunity has been instrumental in expanding my understanding and expertise in experimental particle physics. I hope to continue with this work, specifically aiming to gather more data to increase the statistics and facilitate a more comprehensive comparison between simulation data and real data acquisition.

Acknowledgements

I would like to thank FermiLab and the $g-2$ collabroation for the opportunity to work in the lab and in this experiment. I also want thank my supervisors Prof. Brendan Casey and Dr. Anna Driutti for always being available to help me, and for the all things they taught me about the experiment. I also want to thank Prof. Marco Incagli, Prof. Alberto Lusiani, Prof. Renee Fatemi and the entire simulation team for the constant support in my work. Finally, I would like to thank: Dr. David Tarazona, Dr. Jason Crnkovic and Lorenzo Cotrozzi for the useful discussion and advice.

References

[1] Phys. Rept. **887**, 1 (2020)

[2] Phys. Rev. D **73**, 072003 (2006).

[3] Phys. Rev. Lett. **131**, 161802 (2023).

[4] Chapter 7 of arXiv:1501.06858 (2015).

[5] Nucl. Instrum. Methods A, **945** (2019).

[6] arXiv:2111.02076 (2021).

[7] Phys. Rev. Lett. **126**, 141801 (2021).

[8] See Refs. [3] and [7] for details on the constants used.

[9] Phys. Rev. A **103**, 042208 (2021).

[10] Phys. Rev. D **103**, 072002 (2021).

[11] Chapter 13 of arXiv:1501.06858 (2015).

[12] Phys. Rev. Accel. Beams **24** no.4, 044002 (2021).

[13] J. Phys.: Conf. Ser. **513** 022023 (2014).

[14] Chapter 8 of arXiv:1501.06858 (2015).

[15] Chapter 8 Section 3 of arXiv:1501.06858 (2015).

[16] Link to FermiGrid